Modelling Dispersion in Laminar and Turbulent Flows in an Open Channel based on Centre Manifolds using 1D-IRBFN Method

F.J. Mohammed[a], D. Ngo-Cong[c,*], D.V. Strunin[a,c], N. Mai-Duy[b,c], T. Tran-Cong[b,c]

[a]*School of Agricultural, Computational and Environmental Sciences, Faculty of Health, Engineering and Sciences, University of Southern Queensland, Toowoomba, QLD 4350, Australia.*
[b]*School of Mechanical and Electrical Engineering, Faculty of Health, Engineering and Sciences, University of Southern Queensland, Toowoomba, QLD 4350, Australia.*
[c]*Computational Engineering and Science Research Centre, Faculty of Health, Engineering and Sciences, University of Southern Queensland, Toowoomba, QLD 4350, Australia.*

Abstract

Centre manifold method is an accurate approach for analytically constructing an advection-diffusion equation (and even more accurate equations involving higher-order derivatives) for the depth-averaged concentration of substances in channels. This paper presents a direct numerical verification of this method with examples of the dispersion in laminar and turbulent flows in an open channel with a smooth bottom. The one-dimensional integrated radial basis function network (1D-IRBFN) method is used as a numerical approach to obtain a numerical solution for the original two-dimensional (2-D) advection-diffusion equation. The 2-D solution is depth-averaged and compared with the solution of the 1-D equation derived using the centre manifolds. The numerical results show that the 2-D and 1-D solutions are in good agreement both for the laminar flow and turbulent flow. The maximum depth-averaged concentrations for the 1-D and 2-D models gradually

*Corresponding author. Tel.: +61 414 694 019
Email addresses: Fadhel.Mohammed@usq.edu.au (F.J. Mohammed), Duc.Ngo@usq.edu.au (D. Ngo-Cong), Dmitry.Strunin@usq.edu.au (D.V. Strunin), nam.mai-duy@usq.edu.au (N. Mai-Duy), thanh.tran-cong@usq.edu.au (T. Tran-Cong)

converge to each other, with their velocities becoming practically equal. The obtained numerical results also demonstrate that the longitudinal diffusion can be neglected compared to the advection.

Keywords: Dispersion; Open Channel Flow; Centre Manifolds; Integrated Radial Basis Function; Numerical Method.

1. Introduction

An asymptotic evolution equation governing the cross-flow averaged concentration of contaminants and other substances can be effectively used for prediction of the spreading of the substances in environmental and industrial flows. Taylor [1, 2] constructed an advection-diffusion equation describing the averaged concentration along a channel using half-empirical arguments. The equation is applicable at large times when spatial variations of the concentration along the channel become slow.

A more accurate method of constructing such an equation is based on centre manifold theory; the method was proposed in a series of works (cited below) originated by Roberts. Mercer and Roberts [3] applied the centre manifold theory to describe the dispersion in a laminar flow in a channel. Roberts [4] also showed how to derive appropriate initial conditions for the asymptotic model. In an attempt to obtain more accurate approximations some authors used two-zone models. Chatwin [5] divided the flow into a mean stream layer and a viscous layer near the bottom. Smith [6] derived a delay-diffusion equation in a similar manner to the two-zone model and showed that the results depend on the way the zones are chosen. Chikwendu [7] built a two-zone model with the fast zone in the upper part of the flow and the slow zone near the bottom. He averaged the concentration over each zone separately and described the dynamics in terms of the average concentration in each zone. A system of coupled equations was derived using approximate arguments. Namely, the Newton's law approximated the diffusion through the interface between the zones. Watt and Roberts [8] designed zonal models using techniques closely related to the centre manifold approach. Subsequently, Roberts and Strunin [9] derived a two-zone model based on the centre manifolds. They validated the analysis using direct computations of the original 2-D equations.

Turbulent flows are more difficult to model than laminar ones because, firstly, the turbulent diffusion coefficient depends on the velocity shear and,

secondly, the boundary conditions at the bottom may not be easy to formulate. Strunin [10] analysed the transport of contaminants in turbulent boundary layers of two types. He considered the classical logarithmic velocity profile and, according to an alternative model, power velocity profile. The flow was assumed steady and variations of the contaminant concentration in space and time were supposed slow. The dynamical structure of turbulence was taken into account through the connection between the turbulent diffusion coefficient and the velocity shear.

Our main purpose in the present paper is to justify the averaged model, deduced by the centre manifolds, by direct comparison of numerical solutions of the averaged (1-D) and original (2-D) models, using the one-dimensional integrated radial basis function network (1D-IRBFN) method [11]. The 1D-IRBFN and IRBFN-based methods have been successfully developed and applied to several engineering problems such as structural analysis [12, 13], viscous and viscoelastic flows [14, 15, 16], and fluid-structure interaction [17].

The remainder of the paper is organised as follows. In Section 2, we briefly describe the modelling of dispersion based on centre manifold theory, followed by a discussion of the numerical approach in Section 3. Section 4 discusses the modelling of turbulent dispersion in an open channel. In Section 5, the numerical approach is verified, followed by the discussion on numerical results in Section 6. Section 7 concludes the paper.

2. Modelling dispersion based on Centre Manifold Theory

We consider the 2-D advection-diffusion equation

$$\partial_t c + u(y)\partial_x c = \partial_y[D(y)\partial_y c]\,, \tag{2.1}$$

where $u(y)$ is the velocity of the flow in the channel, supposed known; c the contaminant concentration; and $D(y)$ the diffusion coefficient which is responsible for the turbulent diffusion across the channel and defined by [10]

$$D(y) = K u_*^2/\partial_y u\,, \tag{2.2}$$

in which u_* is the friction velocity and the (non-dimensional and positive) proportionality coefficient K may generally depend on the Schmidt number [18]. The boundary conditions describe non-penetration through the bottom ($y = 0$) and surface ($y = h$, h is the channel height),

$$D\partial_y c|_{y=0} = D\partial_y c|_{y=h} = 0\,. \tag{2.3}$$

We then convert the model (2.1)–(2.3) into the equation for the averaged concentration C_1 using the centre manifolds (Appendix A),

$$\partial_t C_1 = g_1 \partial_x C_1 + g_2 \partial_x^2 C_1 + g_3 \partial_x^3 C_1 \dots . \tag{2.4}$$

The coefficients g_1, g_2 and g_3 are responsible for the advection, diffusion and dispersion, respectively, and are analytically derived as shown in Appendix A.2. We do not include the along-the-flow component of the diffusion, $D_L \partial_x^2 c$, although this can be done without difficulty. In Sub-section 6.3, we show that this term does not affect the averaged model.

Our plan is to solve the original (2-D) transport equation (2.1) with some initial conditions to determine $c(x, y, t)$ after a long elapsed time, then compute the depth-averaged concentration as $C_2(x, t) = \frac{1}{h}\int_0^h c(x, y, t)\, dy$ and compare it with the solution $C_1(x, t)$ obtained from (2.4). As we show in Section 6 the two solutions converge to each other, which confirms the correctness of the averaged model. Several numerical examples on dispersion modelling using the centre manifolds are investigated and reported in Section 6.

3. Numerical Approach: One-Dimensional Radial Basis Function Networks

In this section, we briefly describe the 1D-IRBFN methods [11] including 1D-IRBFN-2 and 1D-IRBFN-4 schemes, with the full details given in Appendix B. The domain of interest is discretised using a Cartesian grid, i.e. an array of straight lines that run parallel to the x- and y-axes as shown in Fig. 1. The dependent variable u and its derivatives on each grid line are approximated using an IRBFN interpolation scheme as described in the remainder of this section.

3.1. Second-order 1D-IRBFN (1D-IRBFN-2 scheme)

Consider an x-grid line, e.g. $[j]$ (Fig. 1). The variation of u along this line is sought in the IRBF form. The second-order derivative of u is decomposed into RBFs; the RBF network is then integrated once and twice to obtain the expressions for the first-order derivative of u and the solution u itself,

$$\frac{\partial^2 u(x)}{\partial x^2} = \sum_{i=1}^{N_x^{[j]}} w^{(i)} G^{(i)}(x) = \sum_{i=1}^{N_x^{[j]}} w^{(i)} H_{[2]}^{(i)}(x)\,, \tag{3.1}$$

$$\frac{\partial u(x)}{\partial x} = \sum_{i=1}^{N_x^{[j]}} w^{(i)} H_{[1]}^{(i)}(x) + p_1 \,, \tag{3.2}$$

$$u(x) = \sum_{i=1}^{N_x^{[j]}} w^{(i)} H_{[0]}^{(i)}(x) + p_1 x + p_2 \,, \tag{3.3}$$

where $N_x^{[j]}$ is the number of nodes on the grid line $[j]$; $\{w^{(i)}\}_{i=1}^{N_x^{[j]}}$ RBF weights to be determined; $\left\{G^{(i)}(x)\right\}_{i=1}^{N_x^{[j]}} = \left\{H_{[2]}^{(i)}(x)\right\}_{i=1}^{N_x^{[j]}}$ known RBFs; $H_{[1]}^{(i)}(x) = \int H_{[2]}^{(i)}(x)dx$; $H_{[0]}^{(i)}(x) = \int H_{[1]}^{(i)}(x)dx$; and p_1 and p_2 integration constants which are also unknown. An example of RBF, used in this work, is the multiquadrics $G^{(i)}(x) = \sqrt{(x - x^{(i)})^2 + a^{(i)2}}$, $a^{(i)}$ - the RBF width determined as $a^{(i)} = \beta d^{(i)}$, β a positive factor, and $d^{(i)}$ the distance from the i^{th} centre to its nearest neighbour. The new basis functions $H_{[1]}^{(i)}(x)$ and $H_{[0]}^{(i)}(x)$ obtained from integrating the multiquadrics $G^{(i)}(x)$ are as follows.

$$H_{[1]}^{(i)}(x) = \frac{r}{2}A + \frac{\left(a^{(i)}\right)^2}{2}B, \tag{3.4}$$

$$H_{[0]}^{(i)}(x) = \left(\frac{r^2}{6} - \frac{\left(a^{(i)}\right)^2}{3}\right)A + \frac{\left(a^{(i)}\right)^2 r}{2}B, \tag{3.5}$$

in which $r = x - x^{(i)}$, $A = \sqrt{r^2 + a^{(i)2}}$, and $B = \ln(r + A)$.

3.2. Fourth-order 1D-IRBFN (1D-IRBFN-4 scheme)

The 1D-IRBFN-4 scheme is used to solve 1-D third- and fourth-order differential equations (Eqs. (4.9) and (6.7)). Consider a 1-D computational domain (a line) with N_x points. The variation of u along this line is sought in the IRBF form. The fourth-order derivative is decomposed into RBFs. The RBF networks are then integrated to obtain the lower-order derivatives and the function itself,

$$\frac{\partial^4 u(x)}{\partial x^4} = \sum_{i=1}^{N_x} w^{(i)} G^{(i)}(x) = \sum_{i=1}^{N_x} w^{(i)} H_{[4]}^{(i)}(x) \,, \tag{3.6}$$

$$\frac{\partial^3 u(x)}{\partial x^3} = \sum_{i=1}^{N_x} w^{(i)} H_{[3]}^{(i)}(x) + p_1 \,, \tag{3.7}$$

$$\frac{\partial^2 u(x)}{\partial x^2} = \sum_{i=1}^{N_x} w^{(i)} H^{(i)}_{[2]}(x) + p_1 x + p_2\,, \tag{3.8}$$

$$\frac{\partial u(x)}{\partial x} = \sum_{i=1}^{N_x} w^{(i)} H^{(i)}_{[1]}(x) + \frac{p_1}{2}x^2 + p_2 x + p_3\,, \tag{3.9}$$

$$u(x) = \sum_{i=1}^{N_x} w^{(i)} H^{(i)}_{[0]}(x) + \frac{p_1}{6}x^3 + + \frac{p_2}{2}x^2 + p_3 x + p_4\,, \tag{3.10}$$

where $\left\{G^{(i)}(x)\right\}_{i=1}^{N_x} = \left\{H^{(i)}_{[4]}(x)\right\}_{i=1}^{N_x}$ are known RBFs; $H^{(i)}_{[3]}(x) = \int H^{(i)}_{[4]}(x)dx$; $H^{(i)}_{[2]}(x) = \int H^{(i)}_{[3]}(x)dx$; $H^{(i)}_{[1]}(x) = \int H^{(i)}_{[2]}(x)dx$; $H^{(i)}_{[0]}(x) = \int H^{(i)}_{[1]}(x)dx$; $\{w^{(i)}\}_{i=1}^{N_x}$ are RBF weights to be determined; and p_1, p_2, p_3 and p_4 integration constants which are also unknown. The new basis functions $H^{(i)}_{[3]}(x)$, $H^{(i)}_{[2]}(x)$, $H^{(i)}_{[1]}(x)$ and $H^{(i)}_{[0]}(x)$ obtained from integrating the multiquadrics $G^{(i)}(x)$ are as follows.

$$H^{(i)}_{[3]}(x) = \frac{r}{2}A + \frac{\left(a^{(i)}\right)^2}{2}B, \tag{3.11}$$

$$H^{(i)}_{[2]}(x) = \left(\frac{r^2}{6} - \frac{\left(a^{(i)}\right)^2}{3}\right)A + \frac{\left(a^{(i)}\right)^2 r}{2}B, \tag{3.12}$$

$$H^{(i)}_{[1]}(x) = \left(-\frac{13\left(a^{(i)}\right)^2 r}{48} + \frac{r^3}{24}\right)A + \left(-\frac{\left(a^{(i)}\right)^4}{16} + \frac{\left(a^{(i)}\right)^2 r^2}{4}\right)B, \tag{3.13}$$

$$H^{(i)}_{[0]}(x) = \left(\frac{\left(a^{(i)}\right)^4}{45} - \frac{83\left(a^{(i)}\right)^2 r^2}{720} + \frac{r^4}{120}\right)A + \left(-\frac{3\left(a^{(i)}\right)^4 r}{48} + \frac{4\left(a^{(i)}\right)^2 r^3}{48}\right)B. \tag{3.14}$$

4. Application to Turbulent Dispersion in an Open Channel

Original 2-D model: Consider a turbulent shear flow in an open channel as presented in [10]. The concentration of contaminant is described by the 2-D advection-diffusion equation (2.1), (hereafter all quantities are non-dimensional)

$$\frac{\partial c}{\partial t} + u(y)\frac{\partial c}{\partial x} = \frac{\partial}{\partial y}\left(D(y)\frac{\partial c}{\partial y}\right)\,, \tag{4.1}$$

where the diffusion coefficient $D(y)$ is represented by (2.2), and the velocity obeys the classical logarithmic law,

$$u(y) = (1/\kappa) \ln (R.y) + B \,, \tag{4.2}$$

where $R = 6000,\ B = 5.5,\ \kappa = 0.4$ and $K = 1$.

The logarithmic law (4.2) is a classical model for turbulent boundary layer described in many books (e.g., [19]). This law is valid in the region $\epsilon < y < 1$ ($\epsilon = 50/R \gg 5/R = h_1/h$, where h_1 is the width of the viscous sublayer). At large Reynolds numbers the value of ϵ is small. Actually, in the present computations we use $\epsilon = 5/R$ but the large Reynolds number $R = 6000$ ensures that both $5/R$ and $50/R$ are small. We note that Eq. (2.4) was derived under the assumption of smallness of ϵ.

We use $B = 5.5$ and $\kappa = 0.4$ because of the following reason: In our analysis, it is convenient that the entire flow from the bottom to the surface is one inertial boundary layer. Using $B = 5.5$ and $\kappa = 0.4$ provides an agreement between the inner and outer regions of the developed boundary flow and ensures that the layer has universal velocity structure [20, 21]. Nikuradse [20] first found the constants $B = 5.5$ and $\kappa = 0.4$ for hydraulically smooth pipe flow. In [21], Keulegan assumed that the same values for these constants can be adopted for smooth open channels. In the literature, these empirical constants can have different values. An extensive survey of mean velocity profile measurements in various 2-D turbulent boundary layer flows by Coles [22] showed that the law of the wall is well represented by equation (4.2) when using $\kappa = 0.4$ and $B = 5.1$. Huffman and Bradshaw [23] used the values $B = 5.0$ and $\kappa = 0.41$. More recently, Steffler et al. [24] adopted the values $B = 5.5$ and $\kappa = 0.4$ and presented some turbulence measurements for uniform flow in a smooth rectangular channel. They found that the velocity measurements in the viscous sublayer agree well with the linear form of the law of the wall.

We consider Eq. (4.1) in a rectangular domain $x_A \le x \le x_B, \epsilon \le y \le 1$ as shown in Fig. 2, subject to the boundary conditions:

$$c = 0, \text{ on } x = x_A \,, \tag{4.3}$$

$$c = 0, \text{ on } x = x_B \,, \tag{4.4}$$

$$\frac{\partial c}{\partial y} = 0, \text{ on } y = \epsilon \,, \tag{4.5}$$

$$\frac{\partial c}{\partial y} = 0, \text{ on } y = 1\,. \tag{4.6}$$

An initial condition is taken in the form of a cloud of the contaminant arbitrarily centered at $x_0 = -11.5$, $y_0 = 1$ (note that $x_A < x_0 < x_B$, and x_A and x_B are set to -100 and 100 at the initial moment, respectively),

$$c(x, y, 0) = \exp\left[-\left(0.1\,(x - x_0)\right)^4 - \left(7(y - y_0)\right)^4\right]. \tag{4.7}$$

The domains of interest are represented by Cartesian grids. Application of the Crank-Nicolson scheme to Eq. (4.1) in conjunction with the use of the 1D-IRBFN method for spatial discretisation results in

$$\frac{c^{(n+1)} - c^{(n)}}{\Delta t} = \frac{F^{(n)}(x, y, t)}{2} + \frac{F^{(n+1)}(x, y, t)}{2}\,, \tag{4.8}$$

where $F(x, y, t) = -u(y)\partial c/\partial x + \kappa K \partial\left(y \partial c/\partial y\right)/\partial y\,.$

Low-dimensional depth-averaged 1-D one-zone model: In the present simulation, we take into account the first four derivatives in the RHS of (2.4) and ignore the higher-order derivatives,

$$\frac{\partial C_1}{\partial t} \approx g_1 \frac{\partial C_1}{\partial x} + g_2 \frac{\partial^2 C_1}{\partial x^2} + g_3 \frac{\partial^3 C_1}{\partial x^3} + g_4 \frac{\partial^4 C_1}{\partial x^4}\,, \tag{4.9}$$

where as shown in [10] $g_1 \approx -(1/\kappa)(\ln R - 1) + B$; $g_2 \approx 1/(4\kappa^3 K)$; and $g_3 \approx 17/(216\kappa^5 K^2)$ for the case of logarithmic velocity profile. In the present paper we also calculate the next coefficient, g_4, through Eqs. (A.10)–(A.13) and obtain $g_4 \approx -65/(4608\kappa^7 K^3)$ as described in detail in Appendix C. Eq. (4.9) is subject to the boundary conditions

$$C_1 = 0, \ \frac{\partial C_1}{\partial x} = 0, \quad \text{at } x = x_A, \ x = x_B\,. \tag{4.10}$$

An initial condition (at $t = t_0$) for Eq. (4.9) is taken to be

$$C_1(x, t_0) = C_2(x, t_0), \tag{4.11}$$

where $C_2(x, t_0) = \frac{1}{(1-\varepsilon)} \int_{\varepsilon}^{1} c\,(x, y, t_0)\, dy$.

The spatial discretisation of first-order and second-order derivatives in Eq. (4.1) is carried out by using (3.1)–(3.2), while the first-order, second-order, third-order and fourth-order derivatives in Eq. (4.9) are discretised through (3.6)–(3.9).

Note that the peak of depth-averaged concentration C (C can be C_1 or C_2) moves along the positive x-axis as time t goes on and the concentration on the inlet and outlet boundaries of the computational domain is assumed to be zero. In order to reduce the computational effort, the computational domain is regularly shifted along the x-axis after a period of time $\Delta\tau$. The strategy to shift the computational domain from time $t = \tau^{(k)}$ to time $t = \tau^{(k)} + \Delta\tau$ is described in Fig. 3. When creating a new computational domain, the inlet boundary is set at the position $x_{A'}$ where $C = \epsilon_C$, presently $\epsilon_C = 10^{-4}$. The concentration in the new region BB'C'C is assigned to be zero at the initial time $t = \tau^{(k)} + \Delta\tau$. The flowchart of numerical procedure is presented in Fig. 4.

5. Verification of the 1D-IRBFN method

Before computing the 1-D and 2-D models using the 1D-IRBFN method and comparing results, we need to verify the method. We consider an artificially constructed advection-diffusion equation with a source function,

$$\frac{\partial c}{\partial t} + u(y)\frac{\partial c}{\partial x} - \frac{\partial^2 c}{\partial y^2} = f(x, y, t)\,, \tag{5.1}$$

where $f(x, y, t) = 2\left(-t/(t^2+1) - xu(y) - 2y^2 + 1\right) e^{-(x^2+y^2)}/(t^2+1)$; and $u(y)$ is given by (4.2). It is easy to check that (5.1) has the analytical solution,

$$c(x, y, t) = e^{-(x^2+y^2)}/(t^2+1). \tag{5.2}$$

We solve Eq. (5.1) numerically in a rectangular domain $-0.5 \le x \le 0.5, \epsilon \le y \le 1$ with $\epsilon = 5/R$ using two cases of boundary conditions:

- Case 1: Dirichlet boundary conditions imposed along all four edges of the rectangular domain.
- Case 2: Dirichlet boundary conditions imposed along two horizontal edges, and Neumann boundary conditions imposed along two vertical edges.

We intend to demonstrate that the numerical solution by the 1D-IRBFN method well agrees with the analytical solution (5.2); this will justify the numerical method.

The boundary and initial conditions must be consistent with (5.2). The initial time moment is taken at $t_0 = 0$. Table 1 and Fig. 5 present the numerical results, namely, the relative error norms (Ne) of the present numerical method for Case 1 and Case 2. The relative error norm is calculated as

$$Ne = \sqrt{\frac{\sum_{i=1}^{N}\left(c^{(i)} - c_a^{(i)}\right)^2}{\sum_{i=1}^{N}\left(c_a^{(i)}\right)^2}}, \tag{5.3}$$

where the subscript "a" denotes the analytical solution; and N is the total number of unknown nodal values in the computational domain. Assuming that the solution is convergent with respect to the grid refinement, the behaviour of the error of the solution is assumed to be $Ne \approx \alpha h^{\lambda} = O(h^{\lambda})$, in which h is the grid spacing; and α and λ the parameters of the exponential model ($\lambda > 0$ is the convergence rate). The convergence behaviour for Case 1 and Case 2 are $O(h^{3.54})$ and $O(h^{2.13})$, respectively. Fig. 6 shows a good agreement between the 1D-IRBFN results of y-average value of the variable c along the x-axis and the analytical solution at several times $t = 1.0, 2.0$ and 3.0.

6. Comparison of 1-D and 2-D dispersion models

6.1. Laminar shear flow in an open channel

Consider a shear flow in an open channel as described by Roberts and Strunin [9], Fig. 7. Note that the direction of the y-axis is opposite to that in Fig. 2 so that the bottom is at $y = 1$ (we follow [9]). The concentration of contaminant obeys the 2-D non-dimensional advection-diffusion equation

$$\frac{\partial c}{\partial t} + u(y)\frac{\partial c}{\partial x} = \frac{\partial^2 c}{\partial y^2}, \tag{6.1}$$

where $u(y) = (3/2)Pe(1 - y^2)$; $Pe = Uh/D$ is the Peclet number, presently set to be 60; U the constant average downstream velocity; h the channel height; and D the constant coefficient of diffusion.

Roberts and Strunin [9] considered two versions of the 2-D model. In the first version, they studied (6.1) in the entire channel domain $x_A \le x \le x_B, 0 \le y \le 1$. They called it a one-zone version. The boundary conditions are

$$c = 0, \text{ on } x = x_A\,, \tag{6.2}$$

$$c = 0, \text{ on } x = x_B\,, \tag{6.3}$$

$$\frac{\partial c}{\partial y} = 0, \text{ on } y = 0\,, \tag{6.4}$$

$$\frac{\partial c}{\partial y} = 0, \text{ on } y = 1\,. \tag{6.5}$$

As in [9], the initial condition is taken in the form

$$c(x, y, 0) = 10 \exp\left[-\left(0.1\,(x - x_0)\right)^4 - \left(7(y - y_0)\right)^4\right]\,, \tag{6.6}$$

with $x_0 = -11.5$, and $y_0 = 0$. The centre manifold theory leads to the following 1-D one-zone model for the flow

$$\frac{\partial C_1}{\partial t} = g_1 \frac{\partial C_1}{\partial x} + g_2 \frac{\partial^2 C_1}{\partial x^2} + g_3 \frac{\partial^3 C_1}{\partial x^3}, \tag{6.7}$$

where $g_1 = -Pe$, $g_2 = Pe^2/30$ and $g_3 = -Pe^3/1575$ [9]. The boundary conditions and the initial condition for (6.7) are taken as (4.10) and (4.11), respectively, in which $c(x, y, t_0)$ is the 2-D concentration from the problem (6.1)–(6.6) at $t = t_0$.

In the second version, Roberts and Strunin [9] subdivided the channel into two zones – slow near the bottom ($\alpha < y \leq 1$) and fast near the surface ($0 \leq y \leq \alpha$), with $\alpha = 0.55$ as shown in Fig. 7. For the cross-zone averaged concentrations in the fast and slow zones, $C_{1f}(x, t)$ and $C_{1s}(x, t)$ respectively, they derived the equations

$$\frac{\partial C_{1f}}{\partial t} = a_1 C_{1f} + a_2 C_{1s} + a_3 \frac{\partial C_{1f}}{\partial x} + a_4 \frac{\partial C_{1s}}{\partial x} + a_5 \frac{\partial^2 C_{1f}}{\partial x^2} + a_6 \frac{\partial^2 C_{1s}}{\partial x^2}\,, \tag{6.8}$$

$$\frac{\partial C_{1s}}{\partial t} = b_1 C_{1f} + b_2 C_{1s} + b_3 \frac{\partial C_{1f}}{\partial x} + b_4 \frac{\partial C_{1s}}{\partial x} + b_5 \frac{\partial^2 C_{1f}}{\partial x^2} + b_6 \frac{\partial^2 C_{1s}}{\partial x^2}\,, \tag{6.9}$$

where $a_1 = -4.441$, $a_2 = 4.441$, $a_3 = -1.397Pe$, $a_4 = 0.0478Pe$, $a_5 = 9.68 \times 10^{-4} Pe^2$, $a_6 = -1.85 \times 10^{-3} Pe^2$; and $b_1 = 5.428$, $b_2 = -5.428$, $b_3 = -0.0461Pe$, $b_4 = -0.527Pe$, $b_5 = -1.78 \times 10^{-3} Pe^2$, $b_6 = 3.34 \times 10^{-3} Pe^2$. The depth-averaged concentration for the whole channel is

$$C_1(x, t) = \alpha C_{1f}(x, t) + (1 - \alpha) C_{1s}(x, t). \tag{6.10}$$

The system of Eqs. (6.8) and (6.9) is subject to the boundary conditions

$$C_{1f} = 0, \ \frac{\partial C_{1f}}{\partial x} = 0, \quad \text{at } x = x_A, \ x = x_B\,, \tag{6.11}$$

$$C_{1s} = 0, \ \frac{\partial C_{1s}}{\partial x} = 0, \quad \text{at } x = x_A, \ x = x_B \, . \tag{6.12}$$

In order to achieve the fastest (exponential) convergence of the 1-D and 2-D models, the following initial conditions were derived by Roberts and Strunin (See [9] for details. A similar derivation is discussed in a simple example in Appendix A.1).

$$\begin{aligned} C_{1f}(x, t_0) \approx & \int_0^1 \left(2.159 - 5.720y^2 + 4.705y^4 - 1.548y^6\right) c\,(x, y, t_0)\, dy \\ & + Pe \int_0^1 \left(-0.010 + 0.174y^2 - 0.482y^4 + 0.494y^6\right) \frac{\partial c\,(x, y, t_0)}{\partial x} dy \, , \end{aligned} \tag{6.13}$$

$$\begin{aligned} C_{1s}(x, t_0) \approx & \int_0^1 \left(-0.417 + 6.991y^2 - 5.750y^4 + 1.892y^6\right) c\,(x, y, t_0)\, dy \\ & + Pe \int_0^1 \left(0.020 - 0.333y^2 + 0.867y^4 - 0.786y^6\right) \frac{\partial c\,(x, y, t_0)}{\partial x} dy \, , \end{aligned} \tag{6.14}$$

where $c(x, y, t_0)$ is, the 2-D concentration from the problem (6.1)–(6.6) at $t = t_0$.

In the following we discuss the numerical results. Fig. 8 shows the contours of the concentration in the channel at times $t = 0.00$ and 0.09 using the 1D-IRBFN method; they are close to those obtained in [9] by finite different method (FDM). A good agreement is also demonstrated in Fig. 9 showing our 1D-IRBFN results and FDM results of [9] for the original (2-D) model and the centre manifold (1-D) models in the one-zone and two-zone versions. The 1D-IRBFN and FDM results correlate well for the slow zone and slightly differ for the fast zone.

Fig. 10 presents the grid convergence study for 2-D analysis of the maximum depth-averaged concentration (C_{max}) with respect to time t. The figure shows that the numerical results obtained are indistinguishable for grids denser than or equal to 81×47. Fig. 11 presents the corresponding grid convergence study for the 1-D one-zone analysis and the converged solution compared with the 2-D and 1-D two-zone results. The figure demonstrates

that the 1-D two-zone solution agrees well with the 2-D model solution while the 1-D one-zone solution is not in very good agreement with the 2-D solution. This is because only three terms (the first-order, second-order and third-order derivatives) are considered in the governing equation of 1-D one-zone model. One can improve the accuracy by including higher-order terms. The maximum depth-averaged concentrations for the 1-D one-zone and 2-D models converge to each other and their velocities along the x-axis are almost the same as indicated by the fact that the curves in Fig. 12 nearly coincide as time increases. The present numerical solutions are obtained at very large times up to $t = 7.0$, rather than at short times around $t = 0.09$, as reported in the work by Roberts and Strunin [9].

6.2. Turbulent shear flow in an open channel

In this example we investigate a shear flow in an open channel governed by Eq. (4.1). Four cases for the 1-D one-zone model are considered here as follows.

- Case 1: Only the advection term ($g_1 \partial C_1/\partial x$) on the RHS of (4.9) is taken into account.
- Case 2: The advection and diffusion terms ($g_1 \partial C_1/\partial x, g_2 \partial^2 C_1/\partial x^2$) on the RHS of (4.9) are taken into account.
- Case 3: The first three leading terms – advection, diffusion and dispersion ($g_1 \partial C_1/\partial x, g_2 \partial^2 C_1/\partial x^2, g_3 \partial^3 C_1/\partial x^3$) on the RHS of (4.9) are taken into account.
- Case 4: The first four leading terms – advection, diffusion, dispersion, and fourth-order dissipation ($g_1 \partial C_1/\partial x$, $g_2 \partial^2 C_1/\partial x^2$, $g_3 \partial^3 C_1/\partial x^3$, $g_4 \partial^4 C_1/\partial x^4$) on the RHS of (4.9) are taken into account.

Fig. 13 compares the distribution of the depth-averaged concentration along the channel between the 2-D model and the 1-D model for the four cases at time $t = 30.0$. It appears that the 1-D Case 1 results are very different from those of the 2-D model while the results of the 1-D Case 2, Case 3 and Case 4 are in good agreement with those of the 2-D model.

Fig. 14 shows the grid convergence study for the 2-D analysis of C_{max} against t. The numerical result is convergent with increasing grid density. The corresponding grid convergence study for the 1-D (Case 4) analysis is also

conducted. We compare the converged 1-D solution with the 2-D solution on a 101×201 grid as shown in Fig. 15. It can be seen that the values of C_{max} for both the 1-D and 2-D models converge to each other as time increases.

6.3. Effect of longitudinal diffusion

It is straightforward to investigate how the longitudinal (along-the-channel) diffusion affects the centre manifold model (A.13)–(A.15). In place of (4.1) we have

$$\frac{\partial c}{\partial t} + u(y)\frac{\partial c}{\partial x} = \frac{\partial}{\partial y}\left(D(y)\frac{\partial c}{\partial y}\right) + D_L\frac{\partial^2 c}{\partial x^2}\,, \tag{6.15}$$

where D_L is the diffusion coefficient along the channel. Instead of (A.6), we now get

$$\partial_t \hat{c} = L[\hat{c}] - iku(y)\hat{c} + (ik)^2 D_L \hat{c}\,. \tag{6.16}$$

Performing the same procedure as in Appendix A.2, we obtain

$$L[\hat{c}] = \frac{\partial \hat{c}}{\partial \hat{C}_1}G + iku\hat{c} - (ik)^2\hat{C}_1\,, \tag{6.17}$$

and, further, upon substitution of (A.9) into (6.17), we get

$$L[\hat{c}] = \sum_{n=1}^{\infty}\sum_{m=1}^{n} c_{n-m}g_m(ik)^n\hat{C}_1 + u(y)\sum_{n=0}^{\infty} c_n(ik)^{n+1}\hat{C}_1 - D_L\sum_{n=0}^{\infty} c_n(ik)^{n+2}\hat{C}_1\,,$$

and, collecting similar terms,

$$L[c_n] = \sum_{m=1}^{n} c_{n-m}g_m + u(y)c_{n-1} - D_L c_{n-2} \quad \text{for } n = 2, 3, \ldots\,. \tag{6.18}$$

When $n = 1$, Eq. (6.18) coincides with (A.12). Integrating (6.18) over the depth, we obtain

$$D(y)\partial_y c|_{y=h} - D(y)\partial_y c|_{y=0} = g_n + \overline{u(y)c_{n-1}} - D_L\overline{c_{n-2}}\,,$$

where, as before, the overbar means depth-average. Since the fluxes through the boundaries are zero, we have

$$g_n = -\overline{u(y)c_{n-1}} + D_L\overline{c_{n-2}} \quad \text{for } n = 2, 3, \ldots$$

Note that the only effect of D_L is the addition to the diffusion coefficient g_2, because $\overline{c_{n-2}} = 0$ for all n except $n = 2$ for which $\overline{c_0} = 1$. For the

logarithmic velocity profile $g_2 \approx 1/(4\kappa^3 K) + D_L$. Using $K = 1$, $\kappa = 0.4$ and $D_L = 0.05$ (according to Taylor [2]), we estimate the ratio between the longitudinal diffusion coefficient and the diffusion coefficient due to the shear $D_L/(1/4\kappa^3 K) = 0.0128$. The small influence of D_L on the concentration dynamics is illustrated by Fig. 16, showing the maximum concentration C_{max} versus time for the 1-D and 2-D models. It can be seen that the effect of the turbulent longitudinal dispersion is indeed small compared to the role of the shear. This supports the modelling of Roberts and Strunin [9] and Strunin [10] who ignored the longitudinal diffusion from the very beginning.

7. Conclusion

The shear dispersion of contaminant based on centre manifold theory is successfully simulated by using the 1D-IRBFN method. The numerical solution of the derived 1-D (one-zone and two-zone) model equations obtained by centre manifolds for both laminar and turbulent flows are in a good agreement with that of the original 2-D advection-diffusion equation. These models yield almost the same velocities of the maximum depth-averaged concentration along the channel. We obtain the 1D-IRBFN solution for the maximum depth-averaged concentration for the 1-D one-zone model taking into account several leading terms including advection, diffusion and dispersion. The solution converges to that of the original 2-D model. A small gap between the solutions exists, however, the accuracy of the centre manifold equation can be improved by including higher-order derivatives. The numerical results confirm that the effect of longitudinal diffusion is negligible. Note that our work can be viewed not only as the confirmation of the centre manifold approach by the 1D-IRBFN technique but also as another confirmation of the numerical technique by the centre manifolds. Our results demonstrate that convergence takes place even for unmodified initial condition as discussed in Appendix A.1.

Acknowledgement

D. Ngo-Cong wishes to thank the University of Southern Queensland for a post-doctoral fellowship. The authors would like to thank the referees for their helpful comments.

References

[1] G. I. Taylor, Dispersion of soluble matter in solvent flowing slowly through a tube, Proc. Roy. Soc. Lond. A 219 (1953) 186–203.

[2] G. I. Taylor, The dispersion of matter in turbulent flow through a pipe, Proc. Roy. Soc. Lond. A 223 (1954) 446–468.

[3] G. N. Mercer, A. J. Roberts, A centre manifold description of contaminant dispersion in channels with varying flow properties, SIAM J. Appl. Math. 50 (1990) 1547–1565.

[4] A. J. Roberts, Appropriate initial conditions for asymptotic descriptions of the long term evolution of dynamical systems, J. Austral. Math. Soc. Ser. B 31 (1989) 48–75.

[5] P. C. Chatwin, A calculation illustration the effects of the viscous sublayer on longitudinal dispersion, Q. Jl Mech. Appl. Math. 26 (1973) 363–378.

[6] R. Smith, A delay-diffusion describtion for contaminant dispersion, J. Fluid Mech. 105 (1981) 469–486.

[7] S. C. Chikwendu, G. U. Ojiakor, Slow-zone model for longitudinal dispersion in two-dimensional shear flows, J. Fluid Mech. 152 (1985) 15–38.

[8] S. D. Watt, A. J. Roberts, The accurate dynamic modelling of contaminant dispersion in channels, SIAM J. Appl. Math. 55 (1995) 1016–1038.

[9] A. J. Roberts, D. V. Strunin, Two-zone model of shear dispersion in a channel using centre manifolds, Q. Jl Mech. Appl. Math. 57 (3) (2004) 363–378.

[10] D. V. Strunin, Universality of turbulent dispersion in a steady flow in an open channel, Q. Jl Mech. Appl. Math. 64 (2) (2011) 197–214.

[11] N. Mai-Duy, R. I. Tanner, A collocation method based on one-dimensional RBF interpolation scheme for solving PDEs, Int. J. Numer. Meth. Heat Fluid Flow 17 (2) (2007) 165–186.

[12] P. B. H. Le, T. Rabczuk, N. Mai-Duy, T. Tran-Cong, A moving IRBFN-based integration-free meshless method, Comput. Model. Eng. Sci. 61 (1) (2010) 63–109.

[13] D. Ngo-Cong, N. Mai-Duy, W. Karunasena, T. Tran-Cong, Free vibration analysis of laminated composite plates based on FSDT using one-dimensional IRBFN method, Comput. Struct. 89 (2011) 1–13.

[14] D. Ngo-Cong, N. Mai-Duy, W. Karunasena, T. Tran-Cong, Local moving least square - one-dimensional IRBFN technique for incompressible viscous flows, Int. J. Numer. Methods Fluids 70 (2012) 1443–1474.

[15] D. Ho-Minh, N. Mai-Duy, T. Tran-Cong, Simulation of viscous and viscoelastic flows using a RBF-Galerkin approach, Aust. J. Mech. Eng. 9 (2) (2012) 101–112.

[16] C.-D. Tran, N. Mai-Duy, K. Le-Cao, T. Tran-Cong, A continuum-microscopic method based on IRBFs and control volume scheme for viscoelastic fluid flows, Comput. Model. Eng. Sci. 85 (6) (2012) 499–519.

[17] D. Ngo-Cong, N. Mai-Duy, W. Karunasena, T. Tran-Cong, A numerical procedure based on 1D-IRBFN and local MLS-1D-IRBFN methods for fluid-structure interaction analysis, Comput. Model. Eng. Sci. 83 (5) (2012) 459–498.

[18] G. I. Barenblatt, Transfer of a passive additive in a turbulent boundary layer at very large Reynolds numbers, Proc. Natl. Acad. Sci. U. S. A. 100 (2003) 1481–1483.

[19] A. S. Monin, A. M. Yaglom, Statistical Fluid Mechanics, Volume II: Mechanics of Turbulence, The MIT Press, Cambridge, US, 1975.

[20] J. Nikuradse, Gesetzmassigkeiten der turbulenten stromung in glatten rohren, Forschung auf d. Gebiete d. Ingenieurwesens 356 (1932) 36 pages.

[21] G. H. Keulegan, Laws of turbulent flows in open channels, J. Res. Natl. Bur. Stand. 21 (6) (1938) 707–741.

[22] D. Coles, The law of the wake in the turbulent boundary layer, J. Fluid Mech. 1 (1956) 191–226.

[23] G. D. Huffman, P. Bradshaw, A note on von Kármán's constant in low Reynolds number turbulent flows, J. Fluid Mech. 53 (1972) 45–60.

[24] P. M. Steffler, N. Rajaratnam, A. W. Peterson, LDA measurements in open channel, J. Hydraul. Eng. 111 (1) (1985) 119–130.

[25] J. Carr, Applied Mathematical Sciences, Volume 35: Applications of Centre Manifold Theory, Springer-Verlag, New York, US, 1981.

Table 1: Two-dimensional advection-diffusion equation with source: Grid convergence study for 1D-IRBFN method at time t = 2.0, using a time step $\Delta t = 5.10^{-3}$.

Grid	Ne	
	Case 1	Case 2
21x21	9.01E-06	1.15E-03
31x31	2.58E-06	4.96E-04
41x41	9.82E-07	2.70E-04
51x51	4.14E-07	1.66E-04
61x61	1.75E-07	1.09E-04

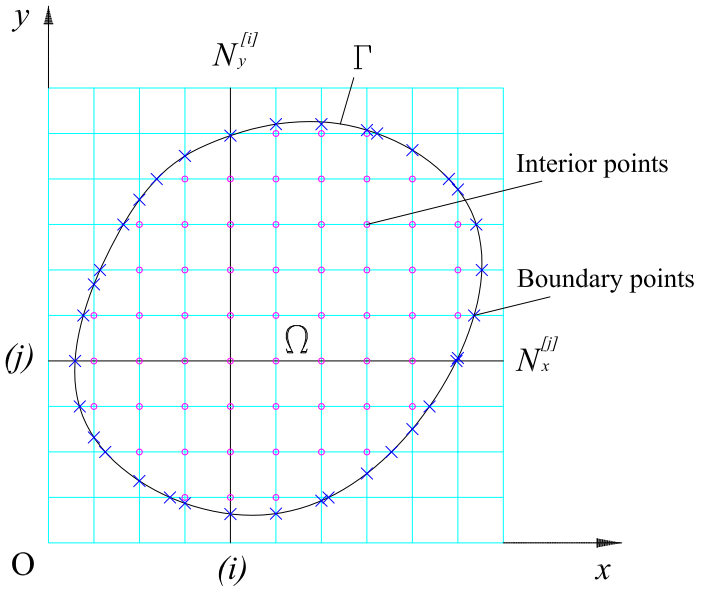

Fig. 1: Cartesian grid.

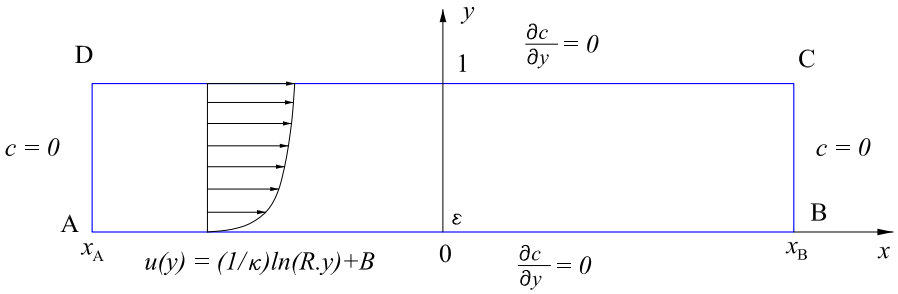

Fig. 2: Shear flow in an open channel [10]: Problem geometry and boundary conditions.

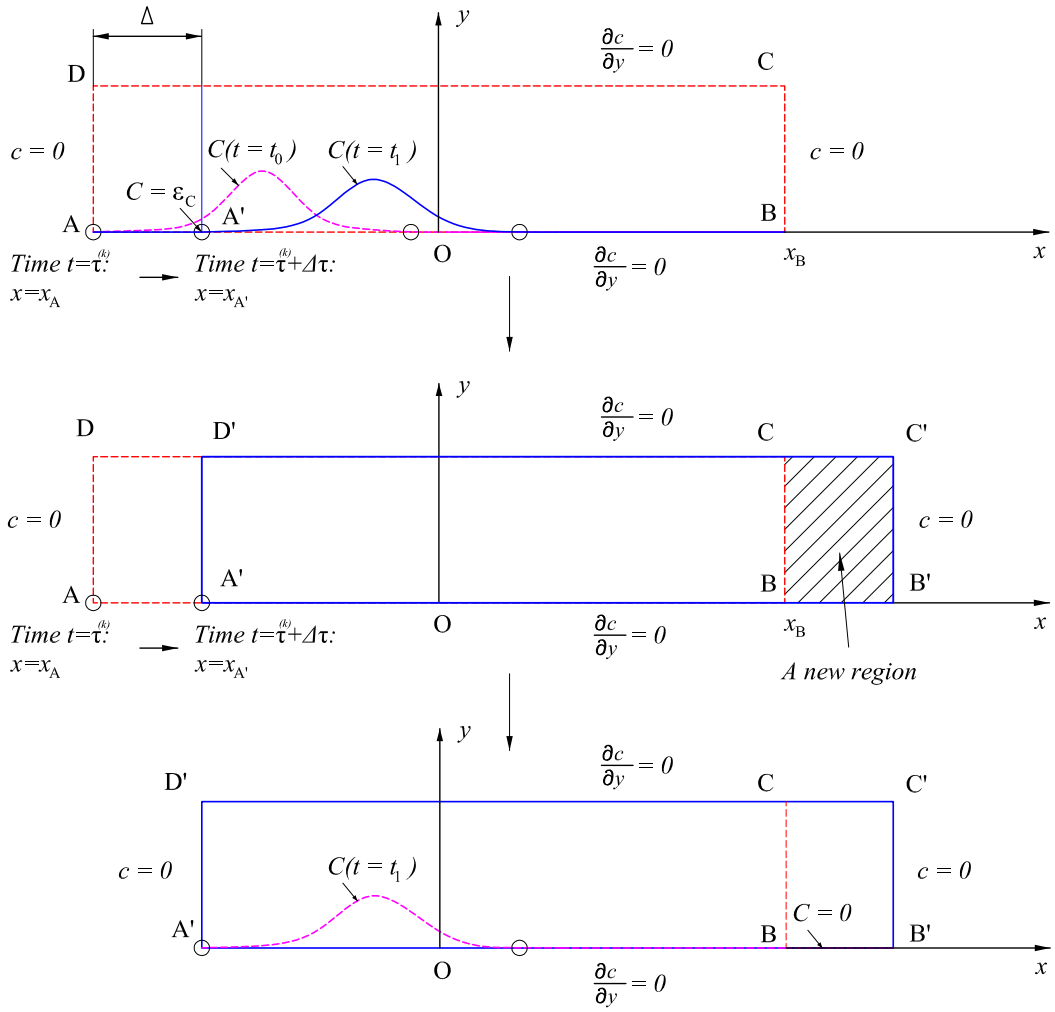

Fig. 3: Shear flow in an open channel: The computational domain is shifted along the x-axis from time $t = \tau^{(k)}$ to time $t = \tau^{(k)} + \Delta\tau$.

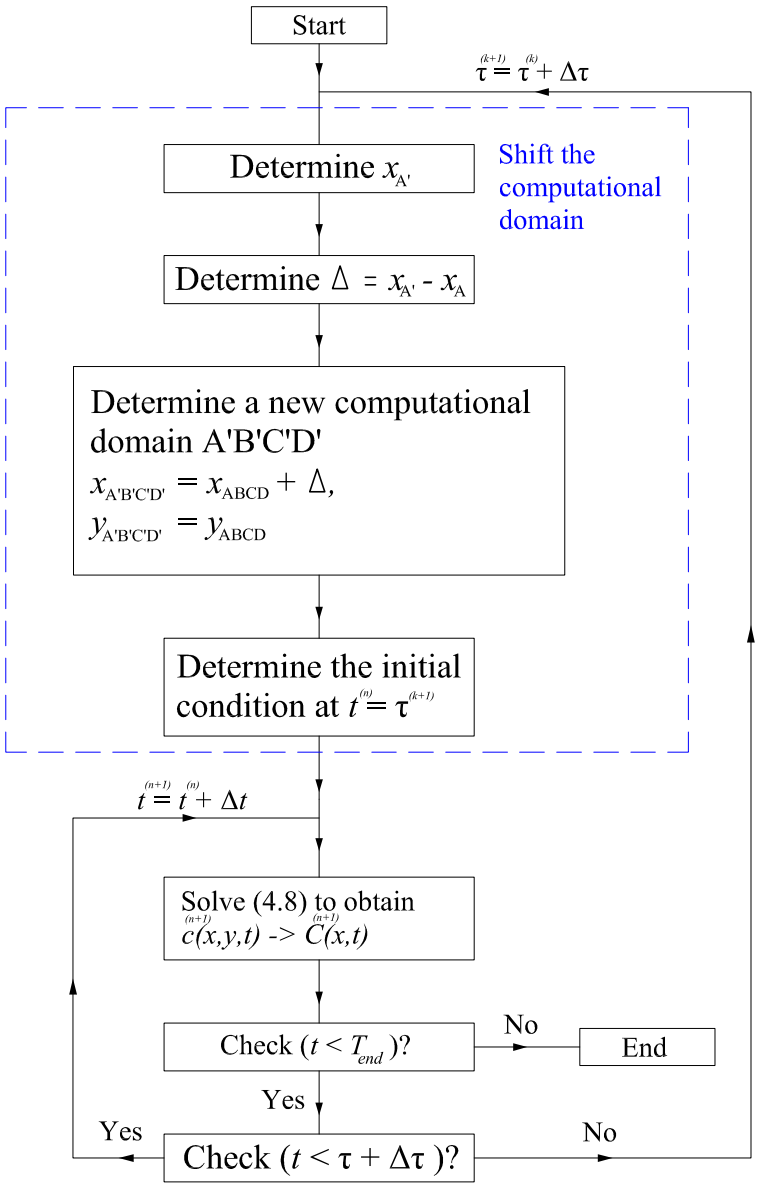

Fig. 4: Flowchart of the numerical analysis.

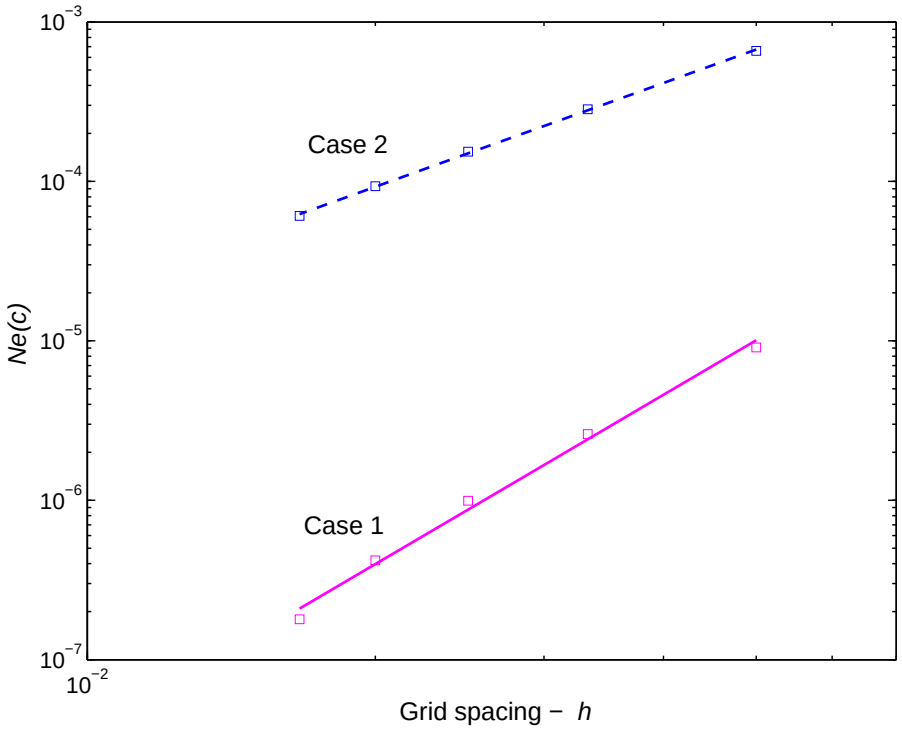

Fig. 5: 2-D advection-diffusion equation with source: Convergence study for 1D-IRBFN method, using a time step $\Delta t = 5.10^{-3}$. The convergence behaviour of 1D-IRBFN for Case 1 and Case 2 are $O(h^{3.54})$ and $O(h^{2.13})$, respectively .

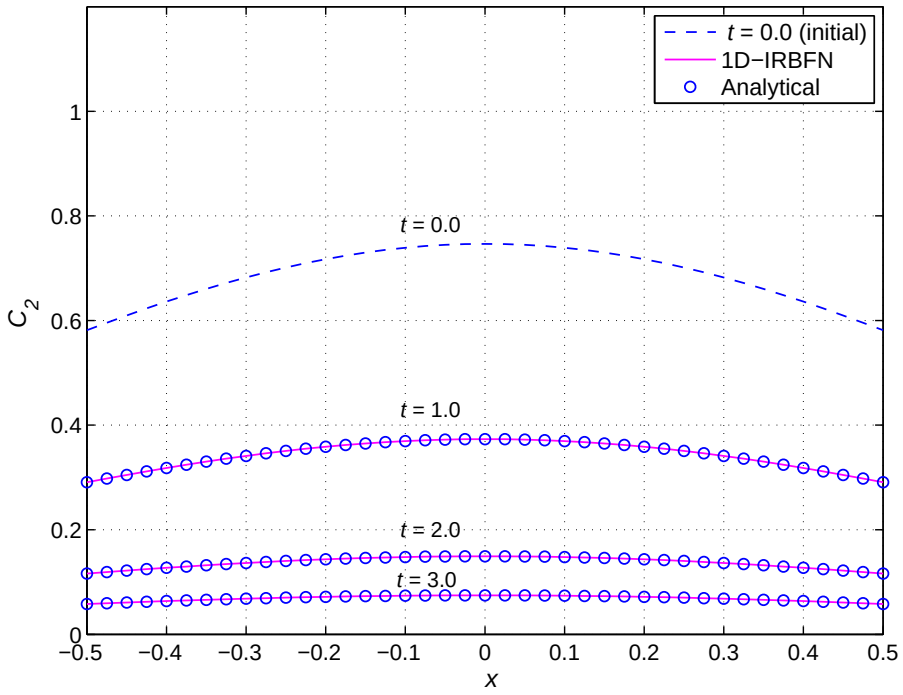

Fig. 6: 2-D advection-diffusion equation with source (Case 2): Comparison of y-average value of variable c (C_2) along the x-axis between the analytical solution and 1D-IRBFN result at several times $t = 1.0, 2.0$ and 3.0, using a time step $\Delta t = 5.10^{-3}$ and a grid of 41×41.

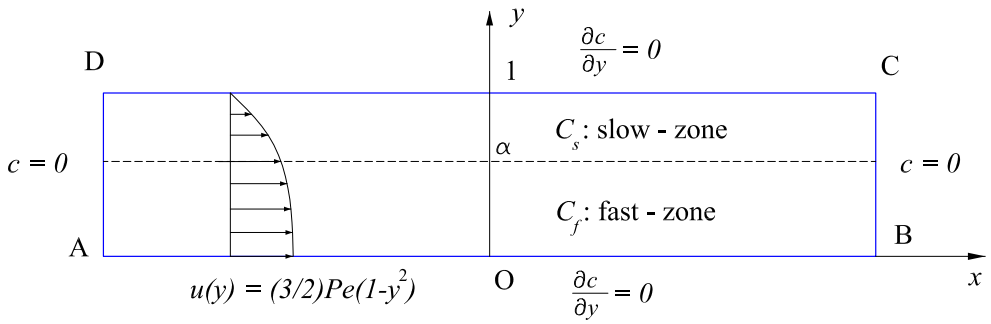

Fig. 7: Laminar shear flow in an open channel: Problem geometry and boundary conditions.

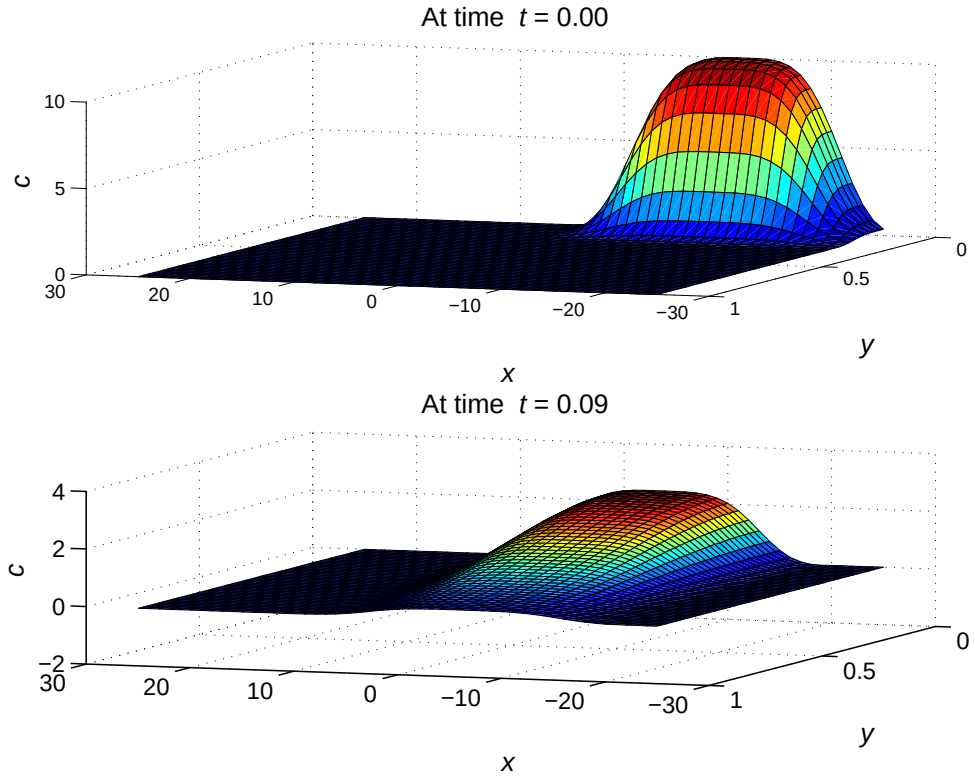

Fig. 8: Laminar shear flow in an open channel: Concentration field in the channel at times $t = 0.00$ and 0.09, using a time step $\Delta t = 0.005$.

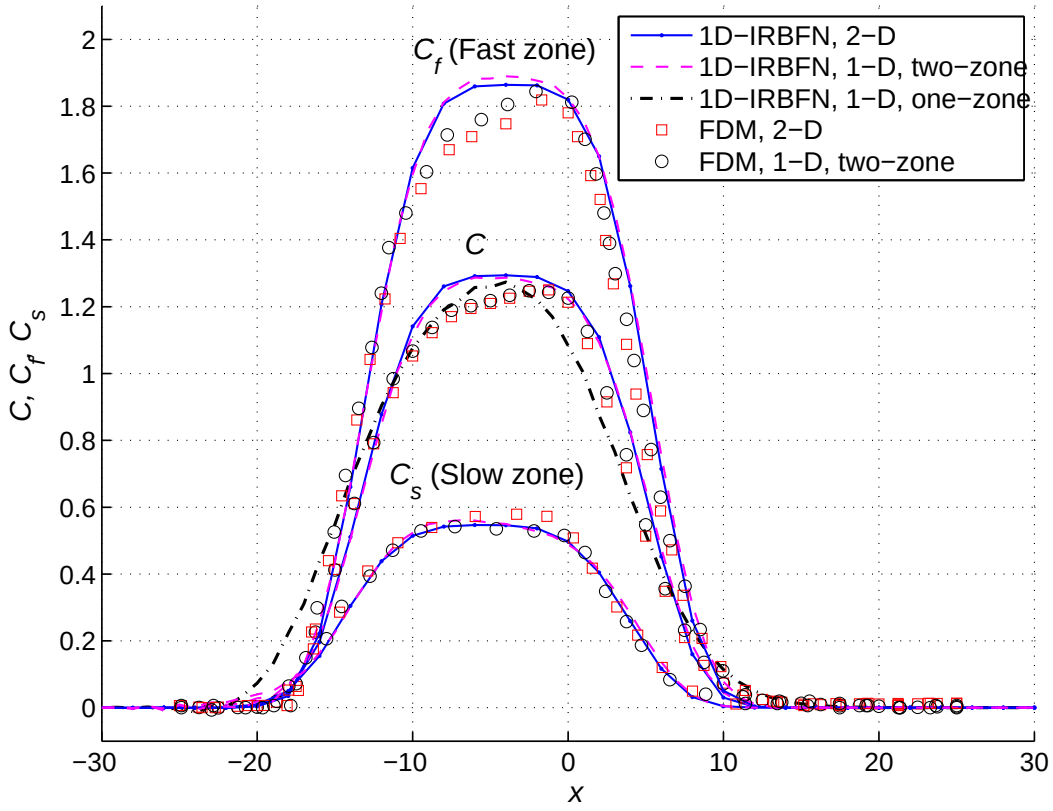

Fig. 9: Laminar shear flow in an open channel: Comparison between 1D-IRBFN and FDM [9] results of the original (2-D) model, the 1-D two-zone model and the 1-D one-zone model at time $t = 0.09$, using a time step $\Delta t = 0.005$. Note that the initial condition is taken at time $t = 0.0$ for both 1-D and 2-D analyses.

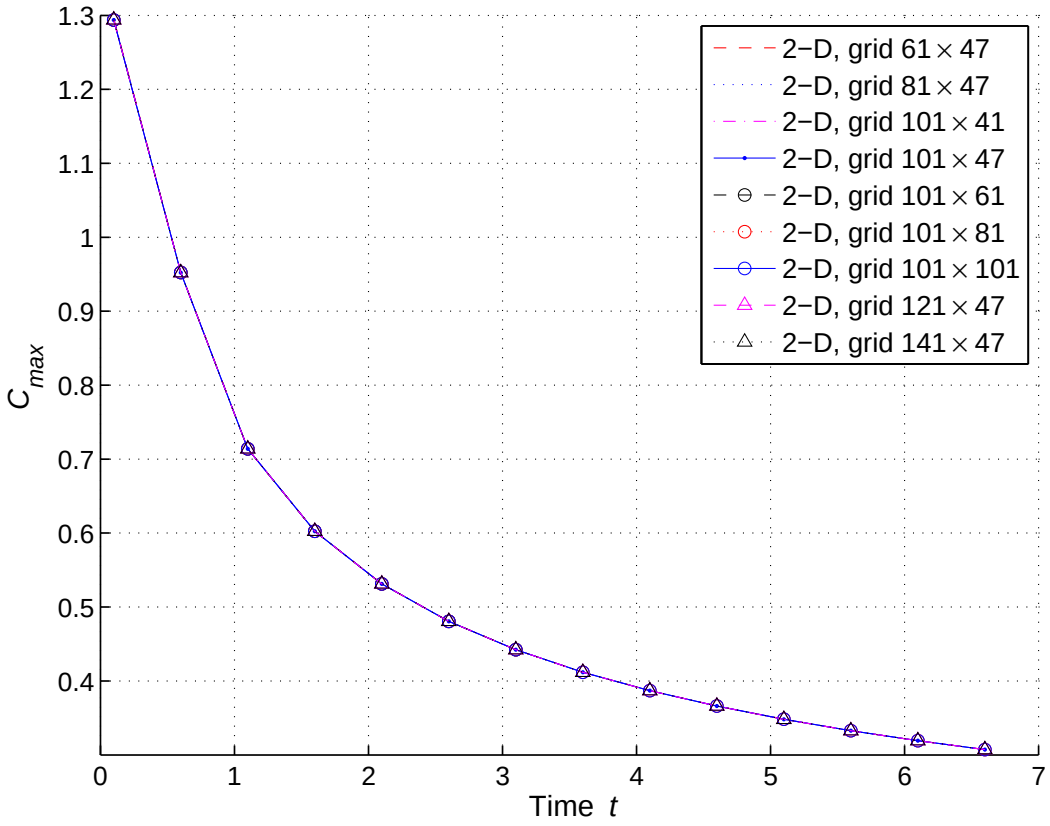

Fig. 10: Laminar shear flow in an open channel: The grid convergence study for 2-D analysis of the maximum depth-averaged concentration with respect to time t, using the 1D-IRBFN method and a time step $\Delta t = 0.005$.

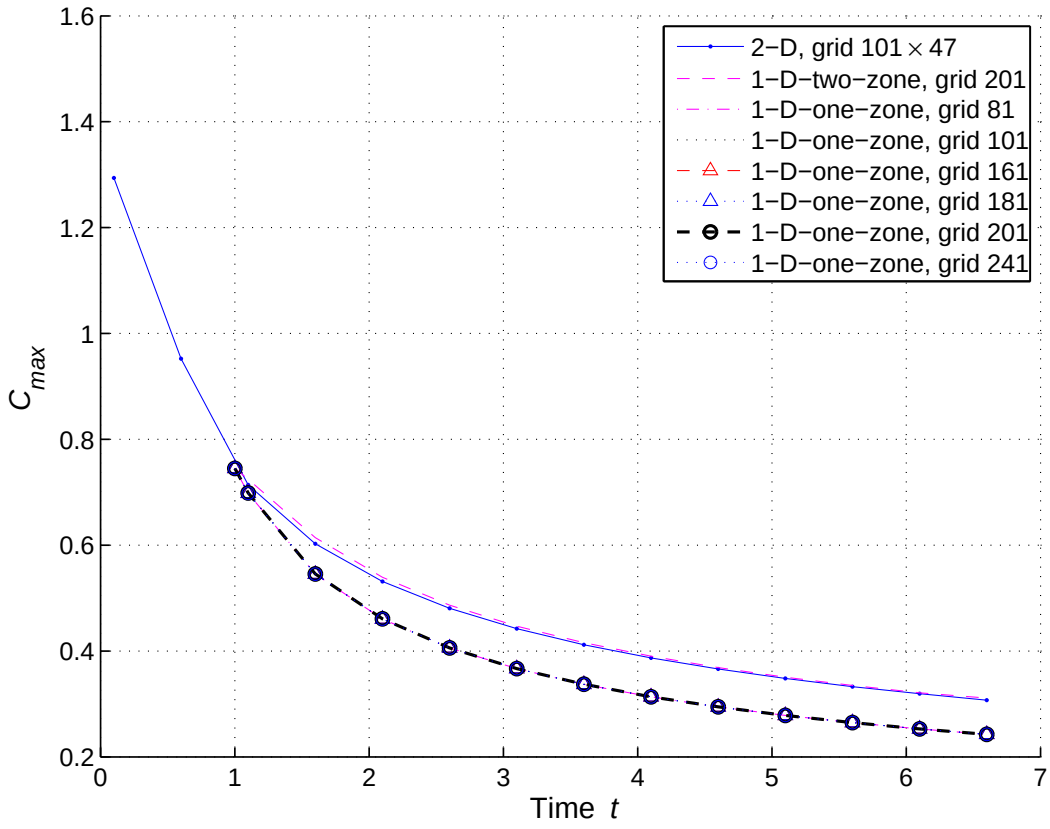

Fig. 11: Laminar shear flow in an open channel: The grid convergence study for 1-D one-zone analysis of the maximum depth-averaged concentration with respect to time t in comparison with the original (2-D) model and the 1-D two-zone model, using the 1D-IRBFN method and a time step $\Delta t = 0.005$. Note that the initial condition is taken at time $t = 1.0$ for 1-D analysis.

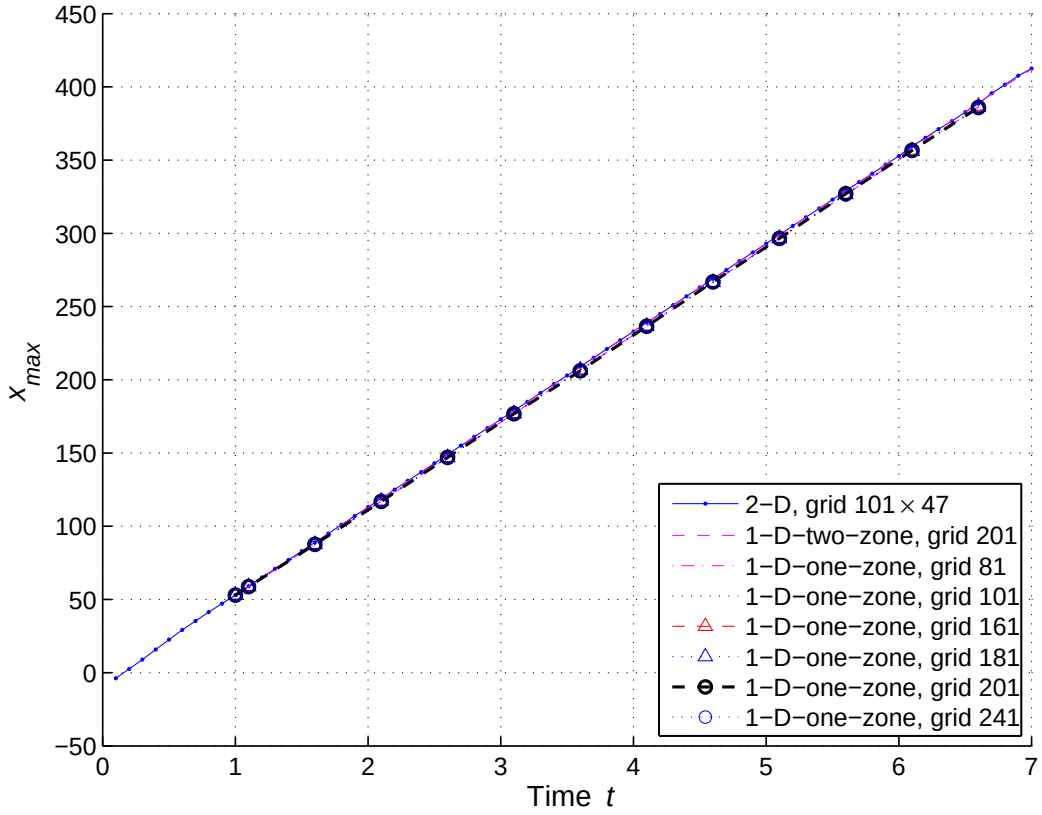

Fig. 12: Laminar shear flow in an open channel: The grid convergence study for 1-D one-zone analysis of the position of the maximum depth-averaged concentration (x_{max}) with respect to time t in comparison with the original (2-D) model and the 1-D two-zone model, using the 1D-IRBFN method and a time step $\Delta t = 0.005$. Note that the initial condition is taken at time $t = 1.0$ for 1-D analysis.

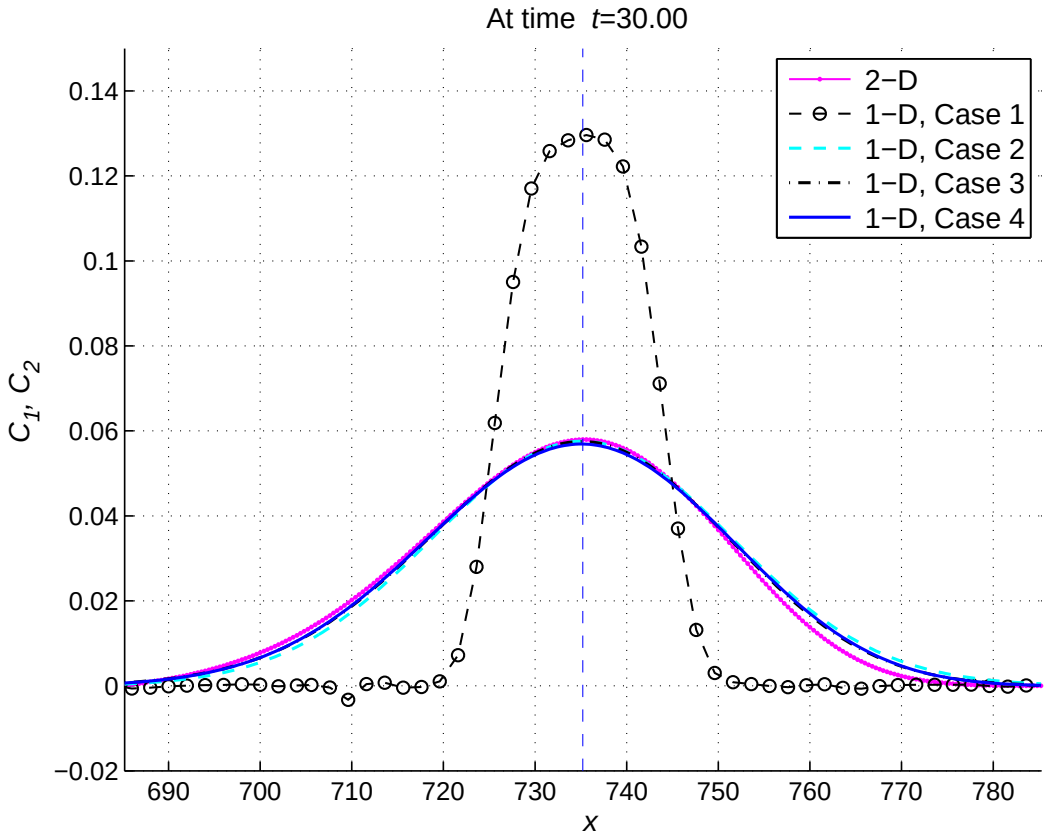

Fig. 13: Turbulent shear flow in an open channel: Comparison of depth-averaged concentration along the channel among the results of the 2-D and 1-D models for Case 1, Case 2 and Case 3 at time $t = 30.00$, using a time step $\Delta t = 5.10^{-3}$ and grids of 101×201 and 201 for 2-D and 1-D analyses, respectively.

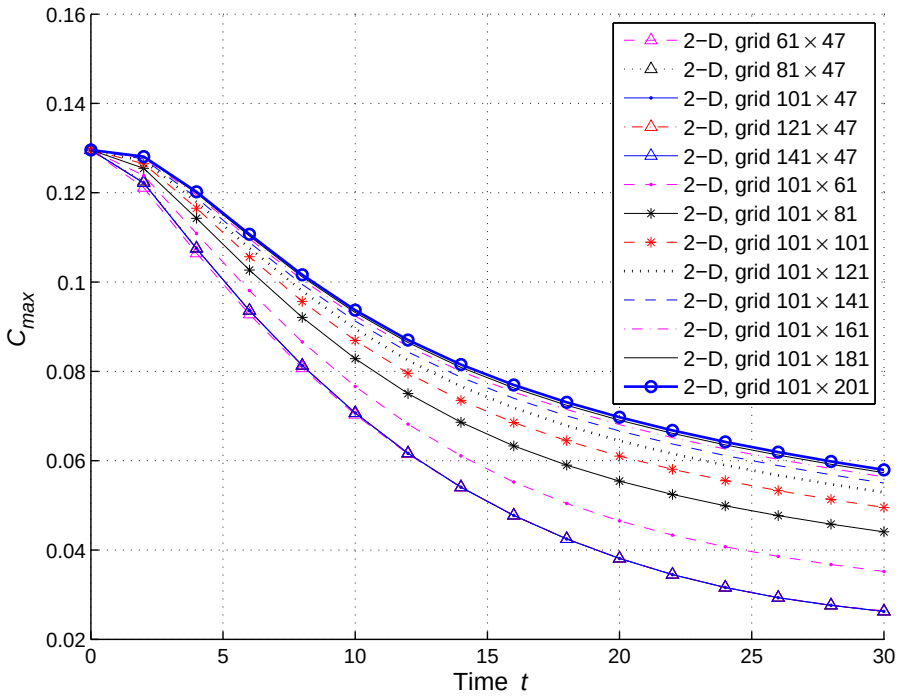

Fig. 14: Turbulent shear flow in an open channel: The grid convergence study for 2-D analysis of the maximum depth-averaged concentration with respect to time t.

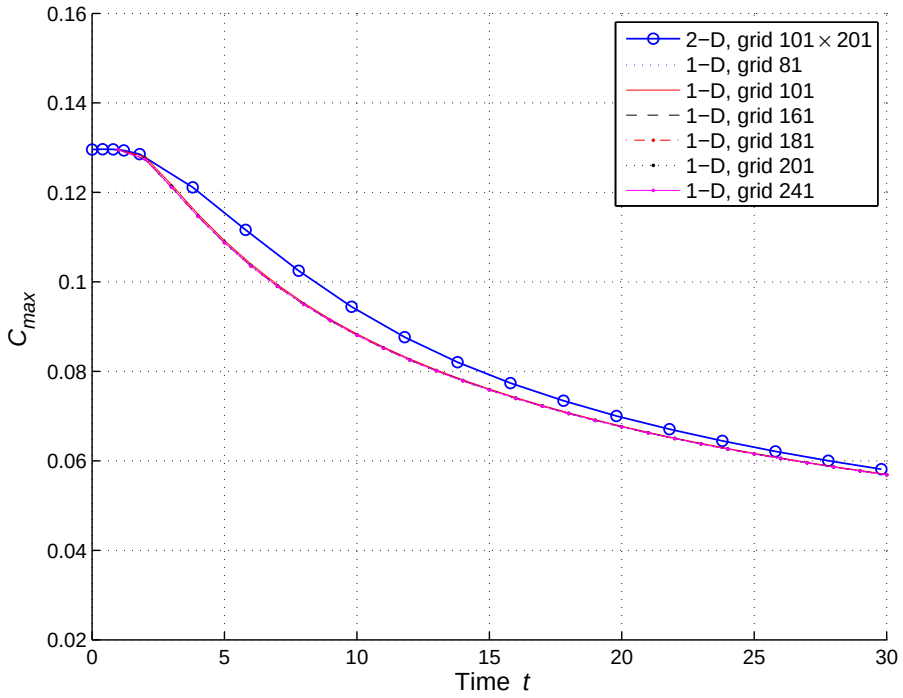

Fig. 15: Turbulent shear flow in an open channel: The grid convergence study for 1-D (Case 4) analysis of the maximum depth-averaged concentration with respect to time t in comparison with the 2-D result. Note that the initial condition is taken at time $t = 1.0$ for 1-D analysis.

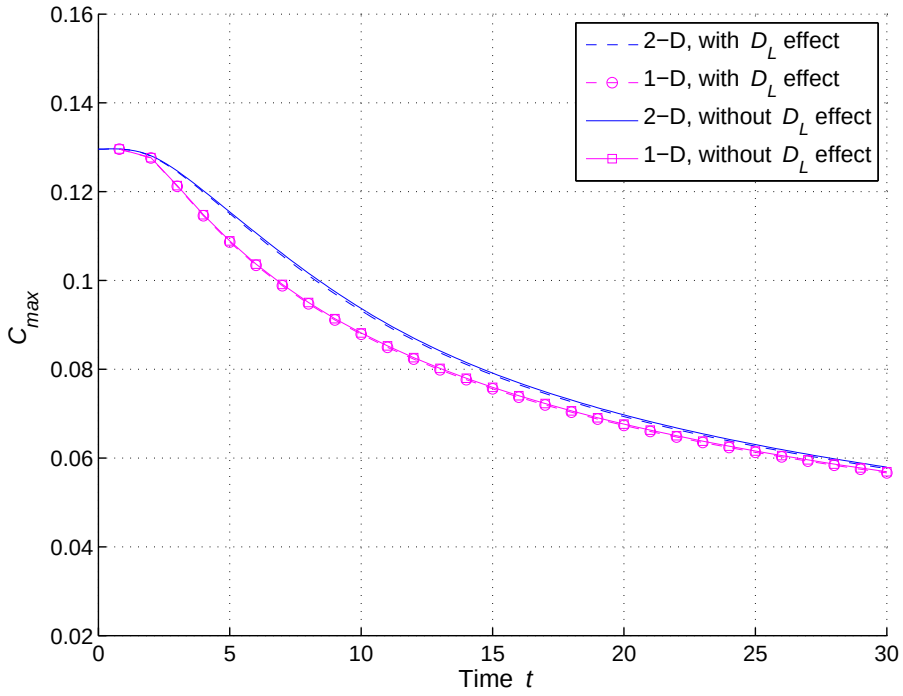

Fig. 16: Turbulent shear flow in an open channel: The influence of longitudinal diffusion on the maximum depth-averaged concentration with respect to time t, using a time step $\Delta t = 5.10^{-3}$ and grids of 101×201 and 201 for 2-D and 1-D analyses, respectively.

Appendix A. Centre Manifold Theory

Appendix A.1. A simple example

The centre manifold theory states that if the linearised state of a continuous-time dynamical system has n zero eigenvalues and m eigenvalues with negative real parts only, then there is a locally defined smooth n-dimensional invariant manifold such that all nearby trajectories of the system are exponentially quickly attracted to the manifold. This manifold is called the centre manifold. We refer to the book of Carr [25] for a detailed description. Below is a simple illustrative example of a centre manifold. Consider the dynamical system from [4],

$$\begin{aligned} da/dt &= -ab\,, \\ db/dt &= -b + a^2 - 2b^2\,. \end{aligned} \tag{A.1}$$

The eigenvalues for the linearised state of the system are 0 and -1. It can be shown that the centre manifold is $b = a^2$ and the motion on it is governed by $da/dt = -a^3$.

For the dynamical system (A.1), Roberts [4] described a procedure to estimate the starting point on the manifold to best match the long term behavior of a trajectory of the system (A.1) which is initially at the point (x_0, y_0) off the centre manifold. Following Roberts, the evolution on a particular trajectory may be written as,

$$x = \left[1/x_0^2 + 2(t+\tau) - \tau e^{-t}/x_0^2\right]^{-1/2} + O(\psi^2)\,, \tag{A.2}$$

where $\tau = (y_0/x_0^2 - 1)\exp(y_0/x_0^2 - 1)$ and ψ has a constant value, which characterizes the trajectory. If the trajectory is on the centre manifold, that is $y_0 = x_0^2$, then $\tau = 0$ and $\psi = 0$ and the evolution on the real trajectory, $x = [1/x_0^2 + 2t]^{-1/2}$, will converge to the centre manifold solution. If the trajectory (A.2) is initially off the centre manifold, then there are two effects on the long term evolution of the system: the effect of the exponential term $-\tau e^{-t}/x_0^2$, which is negligible as time increases, and the effect of the time shift τ. Roberts argued that the time shift τ is a significant long term effect of initially being off the centre manifold. In order to obtain quick convergence, he calculated an initial point different to x_0, say s_0, on the centre manifold which best corresponds to the full system initially being at a

point (x_0, y_0) off the centre manifold. Since the values of x_0 and y_0 are small then $\tau \approx (y_0/x_0^2 - 1)$. Eq. (A.2) can be rewritten as

$$x \approx \left[1/x_0^2 + 2t + 2\tau\right]^{-1/2} + O(\psi^2)\,. \tag{A.3}$$

Now denote $1/x_0^2 + 2\tau$ as $1/s_0^2$. This defines the point on the centre manifold, which is initially at $x = s_0$ and moves so that the actual motion approaches it exponentially quickly. As a result, the solution on the centre manifold converges exponentially quickly to a solution off the centre manifold,

$$x \approx \left[1/s_0^2 + 2t\right]^{-1/2}\,, \tag{A.4}$$

where $s_0 = x_0 - x_0(y_0 - x_0^2) + O(\psi^2)$.

However, it is easy to see that even if the trajectory off the centre manifold starts at (x_0, y_0), then it will converge to the centre manifold after a sufficiently large time. Rewrite Eq. (A.3) as

$$x \approx \frac{1}{\sqrt{2t}}\left[1 + \frac{2\tau + 1/x_0^2}{2t}\right]^{-1/2} + O(\psi^2)$$

which is expanded into the Taylor's series,

$$x \approx \frac{1}{\sqrt{2t}}\left[1 - \frac{2\tau + 1/x_0^2}{4t} + \ldots\right] + O(\psi^2)\,. \tag{A.5}$$

In the limit $t \to \infty$, $x \to 1/\sqrt{2t}$. We can see that $(2\tau + 1/x_0^2)/t$ is the relative discrepancy between $1/\sqrt{2t}$ and Eq. (A.5); it decreases with time. Therefore, the long term evolution of the system (A.1) started off the centre manifold still converges to the centre manifold only not as fast as when it started from $x = s_0$. This is a matter of how long we are willing to wait until the motion settles on the centre manifold. In our problem of dispersion we wait for long enough for the settling to occur. Thus, we do not construct a special initial condition that is similar to $x = s_0$ in the example above. Note that Roberts and Strunin [9] did construct such an initial condition in their dispersion problem.

In the next sub-section, the mechanism of centre manifolds is formalized in the case of dispersion.

Appendix A.2. Dispersion in shear flows with longitudinal diffusion neglected

Consider the flow in a channel. There are two competing factors that govern the distribution of contaminants: (i) the cross-flow diffusion which tends to quickly spread the contaminant in the vertical direction and ensure smooth distribution in this direction; and (ii) the velocity shear which creates non-uniformity of the concentration across the channel, thus acting as an opposite factor to the diffusion. As a result of co-action of these factors, the contaminant evolves relatively slowly in space and time reaching a regime for which the centre manifold approach can be applied. Let us show how this problem is formulated mathematically. Performing the Fourier transformation of (2.1), one gets [3]

$$\partial_t \hat{c} = L[\hat{c}] - iku(y)\hat{c}\,, \tag{A.6}$$

where $\hat{c}(y,k,t)$ is the Fourier transform defined by $\hat{c} = \frac{1}{2\pi}\int_{-\infty}^{\infty} \exp(-ikx)c\,dx$. The linear operator $L[\hat{c}] = \partial_y[D(y)\partial_y\hat{c}]$ expresses the cross-flow turbulent diffusion and has a discrete spectrum of eigenvalues. Consider a simple case of $D(y) = \text{const}$. The diffusion equation for this case, $\partial\hat{c}/\partial t = D\partial^2\hat{c}/\partial y$, complemented by the boundary conditions (2.3), gives $\hat{c} = e^{\lambda t}\cos(\kappa y)$, where the spectrum of eigenvalues λ_m is discrete, $\lambda_m = -D\kappa_m^2$, $\kappa_m = \pi m/h$, $m = 0, 1, ...$ All λ_m are negative except for $\lambda_0 = 0$ corresponding to the neutral eigenmode $\hat{c} = \text{const}$. The negative eigenvalues, λ_m, correspond to decaying non-uniformities of the concentration across the channel due to the diffusion. The case of non-constant diffusion coefficient, $D(y)$, is just a generalization of this case.

We reformulate our dispersion problem to make it similar to Eq. (A.1). After sufficiently long time, variations of the concentration along the channel, that is in x direction, become slow; accordingly we suppose that the wave number k is small. If we add to (A.6) the trivial equation $\partial_t k = 0$, the dynamics exponentially quickly evolve to a low-dimensional state, where each of the fast modes depends on t via the slow neutral mode. As a measure of the "amplitude" of the neutral mode we choose the depth-averaged concentration, $\hat{C}_1$. As a result, we have

$$\hat{c} = \hat{c}(\hat{C}_1, k, y) \quad \text{such that} \quad \partial_t \hat{C}_1 = G(\hat{C}_1, k)\,. \tag{A.7}$$

With (A.7) taken into account, equation (A.6) becomes

$$L[\hat{c}] = \frac{\partial\hat{c}}{\partial\hat{C}_1}G + iku\hat{c}\,. \tag{A.8}$$

Since the problem is linear, we assume linear asymptotic expansions

$$\hat{c} = \sum_{n=0}^{\infty} c_n(y)(ik)^n \hat{C}_1 \,, \quad G = \sum_{n=1}^{\infty} g_n (ik)^n \hat{C}_1 \,. \tag{A.9}$$

The definition of $\hat{C}_1$ as the depth-average implies the conditions

$$\frac{1}{h}\int_0^h c_0 \, dy = 1 \,, \quad \int_0^h c_n \, dy = 0 \quad \text{for } n = 1, 2, \ldots \tag{A.10}$$

Substituting (A.9) into (A.8) and collecting similar terms in powers of the small parameter k we obtain a sequence of equations for the unknown functions $c_n(y)$ and coefficients g_n,

$$L[c_0] = 0 \,, \tag{A.11}$$

$$L[c_n] = \sum_{m=1}^{n} c_{n-m} g_m + u(y) c_{n-1} \quad \text{for } n = 1, 2, \ldots \tag{A.12}$$

Integrating (A.12) over the depth, we get

$$D\partial_y c|_{y=h} - D\partial_y c|_{y=0} = g_n \overline{c_0} + \overline{u(y)c_{n-1}} = g_n + \overline{u(y)c_{n-1}},$$

where the over-bar means depth-average. Since the fluxes through the boundaries are zero

$$g_n = -\overline{u(y)c_{n-1}} \quad \text{for } n = 1, 2, \ldots \tag{A.13}$$

Successively we can calculate g_n and c_n for any n. Considering only three leading terms in the G series in (A.9), we have

$$\partial_t \hat{C}_1 = g_1 (ik)\hat{C}_1 + g_2 (ik)^2 \hat{C}_1 + g_3 (ik)^3 \hat{C}_1 + \ldots \tag{A.14}$$

Now, applying the inverse Fourier transform to (A.14), we obtain the advection-diffusion-dispersion equation for the averaged concentration,

$$\partial_t C_1 = g_1 \partial_x C_1 + g_2 \partial_x^2 C_1 + g_3 \partial_x^3 C_1 + \ldots \tag{A.15}$$

Appendix B. One-Dimensional Radial Basis Function Networks

In this appendix, we use

- the notation $\widehat{[\,]}$ for a vector/matrix $[\,]$ that is associated with a grid line,
- the notation $[\,]_{(\eta,\theta)}$ to denote selected rows η and columns θ of the matrix $[\,]$,
- the notation $[\,]_{(\eta)}$ to pick out selected components η of the vector $[\,]$,
- the notation $[\,]_{(:,\theta)}$ to denote all rows and selected columns θ of the matrix $[\,]$, and
- the notation $[\,]_{(\eta,:)}$ to denote all columns and selected rows η of the matrix $[\,]$.

Appendix B.1. Second-order 1D-IRBFN (1D-IRBFN-2 scheme)

We discuss in detail the formulation on an x-grid line and similar results can be obtained for a y-grid line.

Application of (3.3) at boundary and interior points on the grid line $[j]$ results in

$$\hat{u} = \hat{\mathbf{H}} \begin{pmatrix} \hat{w} \\ \hat{p} \end{pmatrix}, \tag{B.1}$$

where $\hat{\mathbf{H}}$ is an $N_x^{[j]} \times (N_x^{[j]} + 2)$ matrix whose entries are $\hat{H}_{ij} = H_{[0]}^{[j]}(x^{(i)})$, $\hat{u} = (u^{(1)}, u^{(2)}, ..., u^{(N_x^{[j]})})^T$, $\hat{w} = (w^{(1)}, w^{(2)}, ..., w^{(N_x^{[j]})})^T$ and $\hat{p} = (p_1, p_2)^T$. Due to the presence of p_1 and p_2, one can add two additional equations of the form

$$\hat{f} = \hat{\mathbf{K}} \begin{pmatrix} \hat{w} \\ \hat{p} \end{pmatrix} \tag{B.2}$$

to equation system (B.1). For example, in the case of Neumann boundary conditions, this subsystem can be used to impose derivative boundary values

$$\hat{f} = \begin{pmatrix} \frac{\partial u}{\partial x}(x^{(1)}) \\ \frac{\partial u}{\partial x}(x^{(N_x^{[j]})}) \end{pmatrix}, \tag{B.3}$$

$$\hat{\mathbf{K}} = \begin{bmatrix} H_{[1]}^{(1)}(x^{(1)}) & H_{[1]}^{(2)}(x^{(1)}) & ... & H_{[1]}^{(N_x^{[j]})}(x^{(1)}) & 1 & 0 \\ H_{[1]}^{(1)}(x^{(N_x^{[j]})}) & H_{[1]}^{(2)}(x^{(N_x^{[j]})}) & ... & H_{[1]}^{(N_x^{[j]})}(x^{(N_x^{[j]})}) & 1 & 0 \end{bmatrix}. \tag{B.4}$$

The RBF coefficients including two integration constants can be transformed into the meaningful nodal variable values through the following relation

$$\begin{pmatrix} \hat{u} \\ \hat{f} \end{pmatrix} = \begin{bmatrix} \hat{\mathbf{H}} \\ \hat{\mathbf{K}} \end{bmatrix} \begin{pmatrix} \hat{w} \\ \hat{p} \end{pmatrix} = \hat{\mathbf{C}} \begin{pmatrix} \hat{w} \\ \hat{p} \end{pmatrix}, \tag{B.5}$$

or

$$\begin{pmatrix} \hat{w} \\ \hat{p} \end{pmatrix} = \hat{\mathbf{C}}^{-1} \begin{pmatrix} \hat{u} \\ \hat{f} \end{pmatrix}, \tag{B.6}$$

where $\hat{\mathbf{C}}$ is a square conversion matrix of dimension $(N_x^{[j]}+2) \times (N_x^{[j]}+2)$.

By substituting Eq. (B.6) into Eqs. (3.1) and (3.2), the second- and first-order derivatives of the variable u are expressed in terms of nodal variable values

$$\frac{\partial^2 u(x)}{\partial x^2} = \left(H_{[2]}^{(1)}(x), H_{[2]}^{(2)}(x), ..., H_{[2]}^{(N_x^{[j]})}(x), 0, 0 \right) \hat{\mathbf{C}}^{-1} \begin{pmatrix} \hat{u} \\ \hat{f} \end{pmatrix}, \tag{B.7}$$

$$\frac{\partial u(x)}{\partial x} = \left(H_{[1]}^{(1)}(x), H_{[1]}^{(2)}(x), ..., H_{[1]}^{(N_x^{[j]})}(x), 1, 0 \right) \hat{\mathbf{C}}^{-1} \begin{pmatrix} \hat{u} \\ \hat{f} \end{pmatrix}, \tag{B.8}$$

or

$$\frac{\partial^2 u(x)}{\partial x^2} = \bar{D}_{2x} \hat{u} + k_{2x}(x), \tag{B.9}$$

$$\frac{\partial u(x)}{\partial x} = \bar{D}_{1x} \hat{u} + k_{1x}(x), \tag{B.10}$$

where k_{1x} and k_{2x} are scalars whose values depend on x, f_1 and f_2; and $\bar{D}_{1x}$ and $\bar{D}_{2x}$ are known vectors of length $N_x^{[j]}$.

Application of equation (B.9) and (B.10) to boundary and interior points on the grid line $[j]$ yields

$$\widehat{\frac{\partial^2 u^{[j]}}{\partial x^2}} = \hat{\mathbf{D}}_{2x}^{[j]} \hat{u} + \hat{k}_{2x}^{[j]}, \tag{B.11}$$

$$\widehat{\frac{\partial u^{[j]}}{\partial x}} = \hat{\mathbf{D}}_{1x}^{[j]} \hat{u} + \hat{k}_{1x}^{[j]}, \tag{B.12}$$

where $\hat{\mathbf{D}}_{1x}^{[j]}$ and $\hat{\mathbf{D}}_{2x}^{[j]}$ are known matrices of dimension $N_x^{[j]} \times N_x^{[j]}$ and $\hat{k}_{1x}^{[j]}$ and $\hat{k}_{2x}^{[j]}$ are known vectors of length $N_x^{[j]}$.

Similarly, along a vertical line $[j]$ parallel to the $y-$ axis, the values of the second- and first-order derivatives of u with respect to y at the nodal points can be given by

$$\widehat{\frac{\partial^2 u^{[j]}}{\partial y^2}} = \hat{\mathbf{D}}_{2y}^{[j]}\hat{u} + \hat{k}_{2y}^{[j]}, \tag{B.13}$$

$$\widehat{\frac{\partial u^{[j]}}{\partial y}} = \hat{\mathbf{D}}_{1y}^{[j]}\hat{u} + \hat{k}_{1y}^{[j]}. \tag{B.14}$$

Appendix B.2. Fourth-order 1D-IRBFN (1D-IRBFN-4 scheme)

Eq. (3.10) can be written as

$$\hat{u} = \hat{\mathbf{H}} \begin{pmatrix} \hat{w} \\ \hat{p} \end{pmatrix}, \tag{B.15}$$

where $\hat{\mathbf{H}}$ is an $N_x \times (N_x + 4)$ matrix whose entries are $\hat{H}_{ij} = H_{[0]}(x^{(i)})$, $\hat{u} = (u^{(1)}, u^{(2)}, ..., u^{(N_x)})^T$, $\hat{w} = (w^{(1)}, w^{(2)}, ..., w^{(N_x)})^T$ and $\hat{p} = (p_1, p_2, p_3, p_4)^T$. In order to impose Neumann boundary conditions at both ends of the 1-D computational domain ($x = \{x^{(1)},\ x^{(N_x)}, \}$), we add two additional equations of the same form as in (B.2) to equation system (B.15). The RBF coefficients including four integration constants can be transformed into the meaningful nodal variable values through the following relation

$$\begin{pmatrix} \hat{w} \\ \hat{p} \end{pmatrix} = \hat{\mathbf{C}}^{-1} \begin{pmatrix} \hat{u} \\ \hat{f} \end{pmatrix}, \tag{B.16}$$

where $\hat{\mathbf{C}}$ is a non-square conversion matrix of dimension $(N_x + 2) \times (N_x + 4)$ whose inverse can be found using the singular value decomposition (SVD) technique.

By substituting Eq. (B.16) into Eqs. (3.6)–(3.9), the values of derivatives of u with respect to x at the boundary and interior points on the grid line

are obtained as

$$\widehat{\frac{\partial^4 u}{\partial x^2}} = \hat{\mathbf{D}}_{4x}\hat{u} + \hat{k}_{4x}, \tag{B.17}$$

$$\widehat{\frac{\partial^3 u}{\partial x^2}} = \hat{\mathbf{D}}_{3x}\hat{u} + \hat{k}_{3x}, \tag{B.18}$$

$$\widehat{\frac{\partial^2 u}{\partial x^2}} = \hat{\mathbf{D}}_{2x}\hat{u} + \hat{k}_{2x}, \tag{B.19}$$

$$\widehat{\frac{\partial u}{\partial x}} = \hat{\mathbf{D}}_{1x}\hat{u} + \hat{k}_{1x}, \tag{B.20}$$

where $\hat{\mathbf{D}}_{1x}$, $\hat{\mathbf{D}}_{2x}$, $\hat{\mathbf{D}}_{3x}$ and $\hat{\mathbf{D}}_{4x}$ are known matrices of dimension $N_x \times N_x$; and $\hat{k}_{1x}$, $\hat{k}_{2x}$, $\hat{k}_{3x}$ and $\hat{k}_{4x}$ are known vectors of length N_x.

Appendix C. Calculation of g_4 for the logarithmic velocity profile

Substitution of $n = 3$ into Eq. (A.12) leads to

$$L\left[c_3\right] = \sum_{m=1}^{3} c_{3-m} g_m + u\left(y\right) c_{3-1} = c_1 g_2 + c_0 g_3 + c_2[g_1 + u\left(y\right)], \tag{C.1}$$

where $u\left(y\right) = 1/\kappa \ln\left(Re.y\right) + A/u_*$, $c_0 = 1$; and c_1, c_2, g_1, g_2 and g_3 were respectively defined by Strunin [10] as follows.

$$\begin{aligned}
c_1 &= [\frac{1}{K\kappa^2}\left(y\ln y - y\right)], \\
c_2 &= \frac{1}{4K^2\kappa^4}\left(-2y + \frac{y^2}{2} + 3y\ln y - 2y^2\ln y + y^2\ln^2 y + \frac{139}{108}\right), \\
g_1 &= -\frac{1}{\kappa}\left(\ln Re - 1\right) - \frac{A}{u_*},\ g_2 = \frac{1}{4K\kappa^3},\ g_3 = \frac{17}{216K^2\kappa^5}.
\end{aligned}$$

Substituting these functions and coefficients into (C.1), we have

$$\begin{aligned}
\frac{\partial}{\partial y}\left(y\frac{\partial c_3}{\partial y}\right) = \frac{1}{4K^3\kappa^6}\Bigg(&\frac{254}{108} - 3y + \frac{1}{2}y^2 + \frac{139}{108}\ln y + 2y\ln y \\
&-\frac{3}{2}y^2\ln y + 3y\ln^2 y - y^2\ln^2 y + y^2\ln^3 y\Bigg).
\end{aligned} \tag{C.2}$$

Integrating Eq. (C.2) once, we get

$$y\frac{\partial c_3}{\partial y} = \frac{1}{4K^3\kappa^6}\left(\frac{115}{108}y - \frac{5}{4}y^2 + \frac{5}{27}y^3 + \frac{139}{108}y\ln y \right.$$
$$\left. -\frac{1}{2}y^2\ln y - \frac{1}{18}y^3\ln y + \frac{3}{2}y^2\ln^2 y - \frac{2}{3}y^3\ln^2 y + \frac{1}{3}y^3\ln^3 y\right) + B_1. \tag{C.3}$$

Applying the boundary conditions $y\frac{\partial c}{\partial y}|_{y=\epsilon} = y\frac{\partial c}{\partial y}|_{y=1} = 0$ to (C.3), we get $B_1 = 0$. Integrating Eq. (C.3) again, we get

$$c_3 = \frac{1}{4K^3\kappa^6}\left(-\frac{2}{9}y - \frac{1}{8}y^2 - \frac{1}{162}y^3 + \frac{139}{108}y\ln y - y^2\ln y \right.$$
$$\left. +\frac{11}{54}y^3\ln y + \frac{3}{4}y^2\ln^2 y - \frac{1}{3}y^3\ln^2 y + \frac{1}{9}y^3\ln^3 y\right) + B_2. \tag{C.4}$$

Applying the boundary conditions $\int_\epsilon^1 c_n\, dy = 0 \quad for\ n = 1, 2, ...$ to Eq. (C.4), we obtain

$$\frac{1}{4K^3\kappa^6}\left(-\frac{187}{432}y^2 + \frac{1}{8}y^3 - \frac{283}{10368}y^4 + \frac{139}{216}y^2\ln y - \frac{1}{2}y^3\ln y \right.$$
$$\left. +\frac{89}{864}y^4\ln y + \frac{1}{4}y^3\ln^2 y - \frac{5}{48}y^4\ln^2 y + \frac{1}{36}y^4\ln^3 y\right)_\epsilon^1 + B_2 y|_\epsilon^1 = 0. \tag{C.5}$$

Taking the limit $\epsilon \to 0$, we get

$$B_2 = \frac{3475}{41472K^3\kappa^6}.$$

Substitution of the value of B_2 into Eq. (C.4) yields

$$c_3 = \frac{1}{4K^3\kappa^6}\left(\frac{3475}{10368} - \frac{2}{9}y - \frac{1}{8}y^2 - \frac{1}{162}y^3 + \frac{139}{108}y\ln y \right.$$
$$\left. -y^2\ln y + \frac{11}{54}y^3\ln y + \frac{3}{4}y^2\ln^2 y - \frac{1}{3}y^3\ln^2 y + \frac{1}{9}y^3\ln^3 y\right). \tag{C.6}$$

The value of g_4 is then calculated through Eq. (A.13)

$$g_4 = -\overline{u\,(y)\,c_3\,(y)} = -\int_\epsilon^1 \left[\frac{1}{\kappa}\ln\left(Re\, y\right) + \frac{A}{u_*}\right] c_3\, dy$$
$$= -\int_\epsilon^1 \left[\frac{1}{\kappa}\ln Re + \frac{1}{\kappa}\ln y + \frac{A}{u_*}\right] c_3\, dy = -\frac{1}{\kappa}\int_\epsilon^1 c_3\ln y\, dy,$$

or

$$g_4 = -\frac{1}{1-\epsilon}\frac{1}{4K^3\kappa^7}\left(-\frac{3475}{10368}y + \frac{163}{432}y^2 - \frac{25}{216}y^3 + \frac{89}{5184}y^4\right.$$
$$+\frac{3475}{10368}y\ln y - \frac{163}{216}y^2\ln y + \frac{25}{72}y^3\ln y - \frac{89}{1296}y^4\ln y + \frac{139}{216}y^2\ln^2 y \quad \text{(C.7)}$$
$$\left.-\frac{7}{12}y^3\ln^2 y + \frac{29}{216}y^4\ln^2 y + \frac{1}{4}y^3\ln^3 y - \frac{1}{9}y^4\ln^3 y + \frac{1}{36}y^4\ln^4 y\right).$$

Taking the limit $\epsilon \to 0$, we obtain

$$g_4 = -\frac{65}{4608K^3\kappa^7}. \quad \text{(C.8)}$$